Proceedings of The 2019 IEEE International
Conference on Real-time Computing and Robotics
August 4-9, 2019, Irkutsk, Russia

Design of a Cable Driven Floating Robotic Arm with Continuum Joints*

Zhonghao Wu, Marco Cederle, Elisa Rosalinda Giani and Kai Xu*, *Member*, *IEEE*

***Abstract*—Long-reach manipulator shows potentials in inspection, search and rescue. However, the reach of such a manipulator is often limited, due to fact that the distal structures become payloads of the proximal joints. This research hence focuses on a proof-of-concept study of a slim long-reach robotic arm designed with continuum joints and floating links. A float link and a continuum joint constitute a module that is weightless due to buoyancy. The reach hence becomes unlimited in theory. The actuation of each joint is decoupled via a transmission arrangement, providing a simple kinematic model no matter how many robotic modules are used. Each floating link is composed of a from-the-shelf helium-filled Mylar balloon that is caged by acrylic rings. Each of the two-degree-of-freedom continuum joints is made from a super-elastic nitinol (nickel-titanium alloy) rod and actuated by three cables pulled by three stepper motors. Preliminary experimental results on this constructed 3-meter prototype show that the floating robotic arm can move with acceptable accuracy in still air, validating the proposed concept.**

I. Introduction

Long-reach robotic arms are in demand in many application scenarios, such as inspection, cavity detection, search and rescue. Among the existing designs of slim and long-reach robotic arms, two primary approaches were used: i) proximal actuation in which early example can be traced back to the Tensor Arm manipulator [1], ii) modular designs [2, 3].

However, no matter which approach was followed, the weights of the distal structures always become overhead payloads of the proximal joints in terms of actuation and transmission, leading a limited feasible length. Many efforts have hence been put forward to design a lighter structure (e.g., inflatable links).

Using inflated links under pressured gas to form the main structure of a robotic arm is possible way to reduce the weight of such a long-reach manipulator. In the representative designs of inflatable robotic arms, joints formed on or between the compressible links are often bent by actuated tendons [4-8]. It is also possible to utilize gas pressure to actuate these joints [9-11].

However, the inflated links, lighter than the links in the existing designs in [1-3], have non-negligible weights. When the arm becomes longer, the proximal links and joints are still subject to substantial payloads that limit the feasible length of the arm. In order to fundamentally overcome the gravity's influence, floating links were proposed to form long-reach manipulators actuated by thin pneumatic artificial muscles [12-14]. In the aforementioned designs, the kinematics modeling relies on the shape of the structural balloons. Since the balloons are in contact with each other and under the pressure from the actuation muscles, the local deformation of the balloons affect the positioning accuracy of the entire manipulator.

This paper hence proposes a floating robotic arm with continuum joints as shown in Fig.1. It is expected that the closely modelled shapes of the continuum joints and the structural frame of the floating links will contribute to an improved positioning accuracy of the robotic arm.

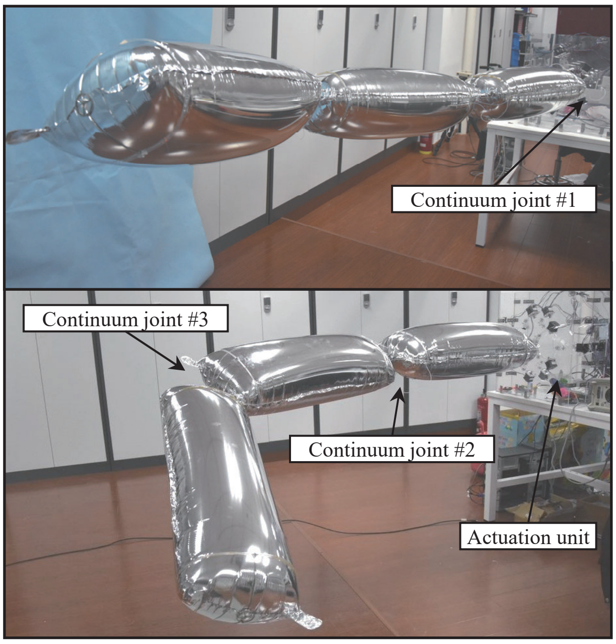

Figure 1. Demonstration of the constructed 3-meter robotic arm with the actuation unit under balancing buoyancy

The paper is organized as follows. Section II presents the design objectives and overview. Section III provides detailed description of the constructed robotic arm system. Kinematics modeling of the robotic arm is derived in Section IV, while experimental validations and actuation compensation are

*This work was supported in part by the National Natural Science Foundation of China (Grant No. 51435010, Grant No. 51722507, Grant No. 51435010, and Grant No. 91648103), and in part by the National Key R&D Program of China (Grant No. 2017YFC0110800).

Zhonghao Wu is with the RII Lab (Lab of Robotics Innovation and Intervention), UM-SJTU Joint Institute, Shanghai Jiao Tong University, Shanghai, China (e-mail: zhonghao.wu@sjtu.edu.cn).

Marco Cederle and Elisa Rosalinda Giani are with the Department of Mechanical Engineering, Politecnico di Milano, Milano, Italy (e-mail: marco.cederle@mail.polimi.it; elisa.giani@mail.polimi.it).

Kai Xu is with the State Key Laboratory of Mechanical System and Vibration, School of Mechanical Engineering, Shanghai Jiao Tong University, Shanghai, China (corresponding author, phone: 86-21-34206547; e-mail: k.xu@sjtu.edu.cn).

reported in Section V. The conclusions and future work are summarized in Section VI.

II. Design Objectives and Overview

To facilitate the development of the floating robotic arms, the design objectives are summarized as follows:

- The design should be lightweight such that buoyancy can balance the arm's weight even with a small payload (e.g., a miniature camera).
- Each module of the arm should be structurally similar. It is preferred that the entire arm has decoupled kinematics (i.e., the actuation of each module is independent from one another).
- The design should be affordable, easy to process and assemble. Maintenance should also be considered.

Inspired by the Giacometti Arm project [12, 13], this paper proposes a feasibility study of a slim long-reach floating robotic arm with continuum joints, as in Fig. 1. An identical floating link and a continuum joint constitute a module, where each joint is bent by three actuation cables that are routed to the actuation unit via flexible guiding cannulas. Flexible cannulas are arranged around each joint to realize a decoupled transmission. In this way, addition of more modules for an increased total length will not affect the actuation kinematics.

The floating links are made from from-the-shelf helium Mylar balloons that are caged by two acrylic rings. Each joint is composed of two stainless steel disk and a thin super-elastic nitinol (nickel-titanium alloy) rod. The 2-DoF (Degree of Freedom) continuum joint can be bent with constant curvature. It is expected that the closely modelled shapes of the continuum joints and the structural frame of the floating links will contribute to an improved positioning accuracy of the robotic arm.

III. Design Descriptions

The floating robotic arm system is composed by floating links, continuum joints and an actuation unit with its transmission.

A. Floating Link

As illustrated in Fig. 2, a helium Mylar balloon is caged by two acrylic spacer rings on both sides. The Mylar balloon has a diameter of 300 mm and a length of 920 mm in its fully inflated status. Once inflated, the link can be considered as a rigid link and will balance a weight of 21 grams.

The two acrylic rings have small holes to provide guidance for the actuation cables. They are connected with each other via three Dyneema cables to be tightened around the Mylar balloon. Using the two acrylic rings, the maintenance can easily be performed, replacing a damaged balloon.

B. Continuum Joint

The continuum joint consists of two stainless steel disks and a nitinol rod in between. The stainless steel disks are connected with the acrylic spacer rings via thin stainless steel spokes. The joint rod is clamped at the centers at the two stainless steel disks. Its role is to enable a constant curvature bending motion, in order to enhance the positioning accuracy. The rod has a diameter of 0.88 mm and a length of 80 mm.

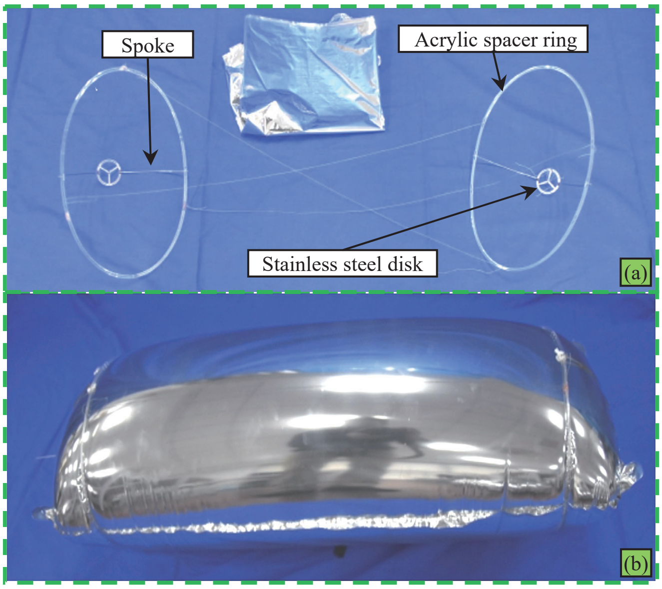

Figure 2. One floating link: (a) acrylic spacer rings, and (b) with inflated helium Mylar balloon

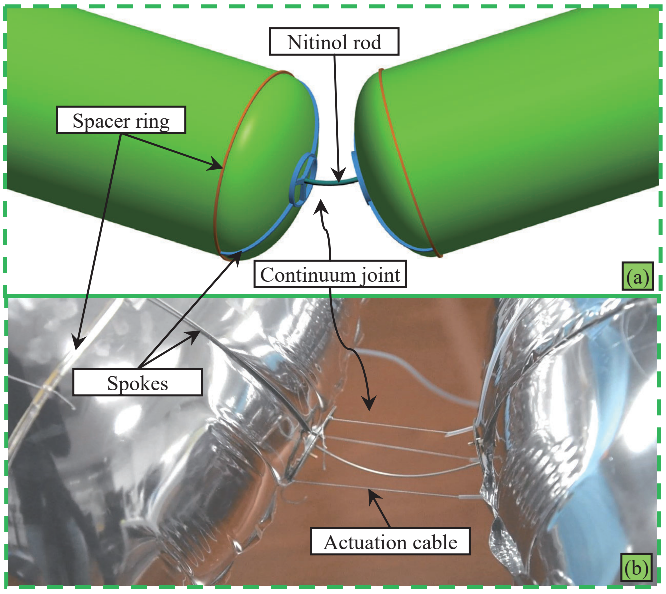

Figure 3. The continuum joint and spacer ring: (a) CAD drawing, and (b) actual prototype

Each stainless steel disk of the continuum joint has a diameter of 40 mm. It has three equidistantly distributed holes for attaching or passing the actuation cables. The actuation cables have a diameter of 0.3 mm and they are considered inextensibility since the load on the actuation cables is relatively low.

The continuum joint is bent by pulling the actuation cables. The cables are tightened to the actuation unit such that the compressed Mylar balloon can provide a level of pre-tension to prevent cable slack. Bending angle and bending direction of the continuum joint can be obtained from the actuated cable lengths, according to the kinematics in Section IV.

Each stainless steel disk of the continuum joint is connected to the spacer ring through two stainless steel spokes as shown in Fig. 2(a) and Fig. 3. The weight of each component is presented in Table I.

TABLE I. WEIGHTS OF COMPONENTS

Component	Material	Weight
Spacer ring	Acrylic plastic	1.99 g
Disk	Stainless steel	5.81 g
Spoke	Stainless steel	0.93 g

C. *Actuation Unit with its Transmission*

Since the cables that drive the distal links will pass through the proximal joints, in order to decouple the actuation, axial incompressible flexible cannulas are arranged in curved shapes around the joint between two adjacent links. In this way, the flexible cannulas will not hinder the bending of the continuum joint, nor affect the actuation lengths of the cables.

Because the lengths of the cannulas are constant, the control of each continuum joint is hence decoupled from one another. This leads to a simpler kinematics for this multi-module robotic arm.

As shown in Fig. 4, the actuation unit is placed at the proximal end of the robotic arm. It has a layered structure made from acrylic boards. The motors for the actuation cables of the same continuum joint are located around a circle on one acrylic board, with a division angle of 120°.

Six stepper motors are arranged at the higher layer with twelve pulleys for the actuation of the 1st and the 2nd continuum joints. Three stepper motors are arranged at the lower layer with six pulleys for the actuation of the 3rd continuum joint. The cables for the 2nd and 3rd joints are distributed around a circle with a larger radius to conform to the external shape of the balloons, while the cables for the 1st joint are around a circle with the same radius of the outer diameter of the stainless steel disks of the joints. Several guiding tubes are placed on the board to form paths for the actuation cables to pass.

IV. KINEMATICS

In the kinematics derivation, the following modeling assumptions are used:

- The super-elastic material nitinol is assumed to have linear and isotropic elasticity.
- The nitinol rod is perpendicular to the base and the end disks, referring to Fig. 6(a).
- Bending of the joints is approximated to be constant curvature, referring to the experimental and theoretical verifications in [15, 16].
- Actuation cables are assumed to be inextensible.

The nomenclature and coordinates are defined in Section IV.A. Referring to Fig. 5, there are three representations of the robotic arm: the joint space, the configuration space and the task space. The mapping between the configuration space and the task space is reported in Section IV.B, while the mapping between the joint space and the configuration space is presented in Section IV.C.

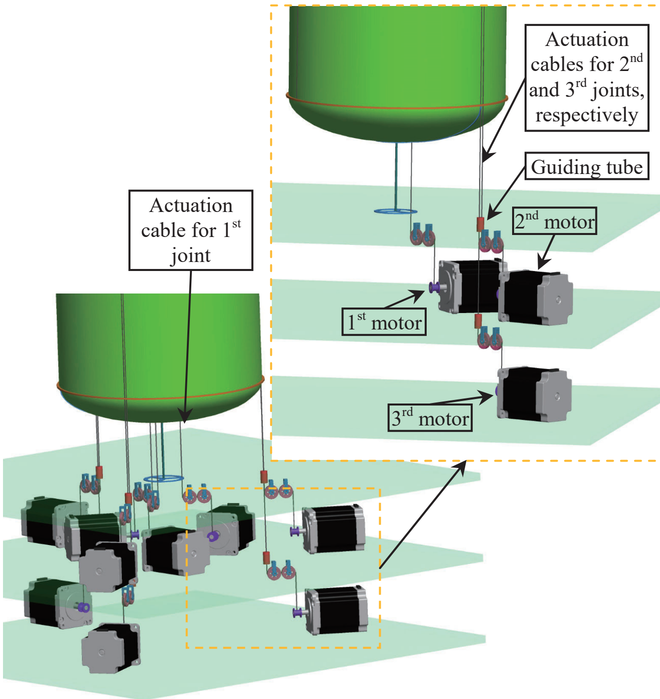

Figure 4. Arrangement of the actuation unit

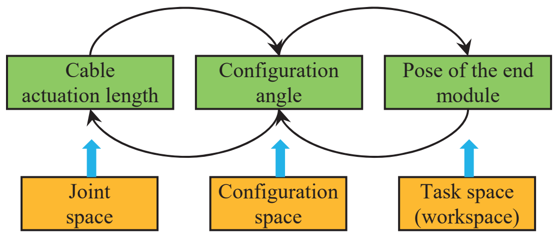

Figure 5. Mapping between different modeling spaces

A. *Nomenclature and Coordinates*

Four coordinates are defined for the t^{th} joint as follows, referring to Fig. 6. And the nomenclature is listed in Table II.

- *Base Disk Coordinate* $\{tb\} \equiv \{\hat{\mathbf{x}}_{tb}, \hat{\mathbf{y}}_{tb}, \hat{\mathbf{z}}_{tb}\}$ is fixed in the center of the base disk with $\hat{\mathbf{z}}_{tb}$ tangent to the central nitinol rod and $\hat{\mathbf{x}}_{tb}$ pointing to the first actuation cable.
- *Proximal Bending Plane Coordinate* $\{t1\} \equiv \{\hat{\mathbf{x}}_{t1}, \hat{\mathbf{y}}_{t1}, \hat{\mathbf{z}}_{t1}\}$ is defined such that the joint bends in the *XY* plane and $\hat{\mathbf{x}}_{t1}$ aligns with $\hat{\mathbf{z}}_{tb}$.
- *Distal Bending Plane Coordinate* $\{t2\} \equiv \{\hat{\mathbf{x}}_{t2}, \hat{\mathbf{y}}_{t2}, \hat{\mathbf{z}}_{t2}\}$ is obtained by rotating $\{t1\}$ around the $\hat{\mathbf{z}}_{t1}$ with an angle of θ_t bringing $\hat{\mathbf{x}}_{t2}$ tangent to the tip of the central nitinol rod, with the origin at the center of the end disk.

- *End Disk Coordinate* $\{te\} \equiv \{\hat{\mathbf{x}}_{te}, \hat{\mathbf{y}}_{te}, \hat{\mathbf{z}}_{te}\}$ is affixed at the center of the end disk with $\hat{\mathbf{z}}_{te}$ perpendicular to the end disk and $\hat{\mathbf{x}}_{t2}$ pointing to the first actuation cable.

TABLE II. NOMENCLATURE USED IN THE KINEMATICS MODELING

Symbol	Definition
t	Index of the modules $t = 1,2,3,\ldots, n$.
j	Index of the actuating cables, $j = 1,2,3$.
r	Radius of the pitch circle defining the positions of the three cables on the stainless steel disk of the t^{th} joint.
β	Division angle for the three actuation cables along the circumference of the pitch circle ($\beta = 120°$).
l_t	Length of central nitinol rod of the t^{th} continuum joint.
h_t	Length of the t^{th} floating link.
$l_{t\,j}$	Length of the j^{th} actuation cable of the t^{th} continuum joint.
θ_t	Bending angle of the central rod (a.k.a., the bending angle of the continuum joint) of the t^{th} joint.
δ_t	For the t^{th} continuum joint, the angle of a right-handed rotation about $\hat{\mathbf{z}}_{tb}$ from $\hat{\mathbf{y}}_{t1}$ to $\hat{\mathbf{x}}_{tb}$.
$\mathbf{q}_t$	$\mathbf{q}_t = [q_{t1}, q_{t2}, q_{t3}]^T$ is the joint space vector of the t^{th} joint.
$\mathbf{\Psi}_t$	$\mathbf{\Psi}_t = [\theta_t, \delta_t]^T$ is the configuration space vector of the t^{th} continuum joint.
${}^{a}\mathbf{p}_b$	A vector pointing from the origin of frame a to the origin of frame b with respect to frame a.
${}^{a}\mathbf{R}_b$	Transformation matrix from frame b to a.

B. Configuration Space Kinematics

Referring to Fig. 6, $\{(t+1)b\}$ is translated from $\{te\}$ by a length of the floating link. Hence the following equation holds.

$$ {}^{tb}\mathbf{R}_{(t+1)b} = {}^{tb}\mathbf{R}_{te} = {}^{tb}\mathbf{R}_{t1}\,{}^{t1}\mathbf{R}_{t2}\,{}^{t2}\mathbf{R}_{te} \tag{1} $$

Where ${}^{tb}\mathbf{R}_{t1} = \begin{bmatrix} 0 & \cos\delta_t & \sin\delta_t \\ 0 & -\sin\delta_t & \cos\delta_t \\ 1 & 0 & 0 \end{bmatrix}$,

${}^{t1}\mathbf{R}_{t2} = \begin{bmatrix} \cos\theta_t & -\sin\theta_t & 0 \\ \sin\theta_t & \cos\theta_t & 0 \\ 0 & 0 & 1 \end{bmatrix}$ and ${}^{t2}\mathbf{R}_{te} = {}^{tb}\mathbf{R}_{t1}^{T}$.

For the continuum joint, the position relationship from the base disk to the end disk can be written as:

$$ {}^{tb}\mathbf{p}_{te} = \frac{l_t}{\theta_t}\begin{bmatrix}\cos\delta_t(1-\cos\theta_t) & \sin\delta_t(\cos\theta_t - 1) & \sin\theta_t\end{bmatrix}^T \tag{2} $$

When θ_t approaches zero, the following expression should be used:

$$ \lim_{\theta_t \to 0} {}^{tb}\mathbf{p}_{te} = \begin{bmatrix} 0 & 0 & l_t \end{bmatrix}^T \tag{3} $$

The floating link gives a translation as follows:

$$ {}^{te}\mathbf{p}_{(t+1)b} = \begin{bmatrix} 0 & 0 & h_t \end{bmatrix}^T \tag{4} $$

Thus, the homogeneous transformation for one module, (namely, a continuum joint with a link), is given by:

$$ {}^{tb}\mathbf{T}_{(t+1)b} = {}^{tb}\mathbf{T}_{te}\,{}^{te}\mathbf{T}_{(t+1)b} = \begin{bmatrix} {}^{tb}\mathbf{R}_{te} & {}^{tb}\mathbf{p}_{te} \\ \mathbf{0}_{3\times1} & 1 \end{bmatrix}\begin{bmatrix} \mathbf{I} & {}^{te}\mathbf{p}_{(t+1)b} \\ \mathbf{0}_{3\times1} & 1 \end{bmatrix} \tag{5} $$

Referring to Fig. 6(b), the homogeneous transformation from the distal module of the robotic arm to the proximal end is derived as:

$$ \mathbf{T} = \left(\prod_{t=1}^{n-1} {}^{tb}\mathbf{T}_{(t+1)b}\right) {}^{nb}\mathbf{T}_{ne}\begin{bmatrix} \mathbf{I} & \begin{bmatrix} 0 & 0 & h_n \end{bmatrix}^T \\ \mathbf{0}_{3\times1} & 1 \end{bmatrix} \tag{6} $$

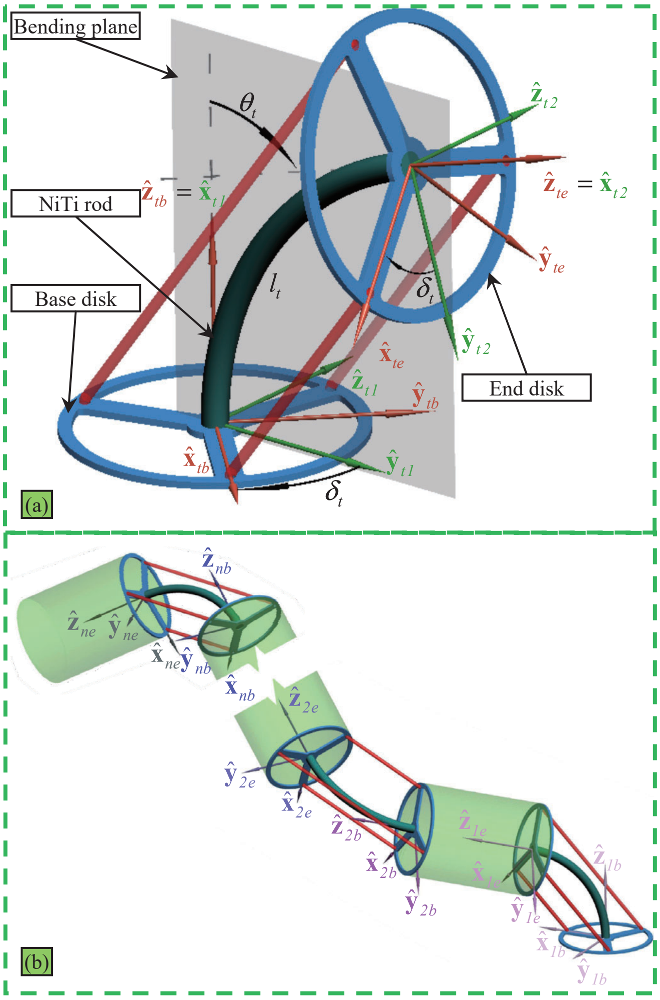

Figure 6. Nomenclature and coordinates: (a) the t^{th} joint, and (b) the n-module robotic arm (in the Section V, n = 1, 2, or 3)

The instantaneous kinematics mapping between the configuration space and the task space is formulated as follows:

$$ \dot{\mathbf{x}}_t = \mathbf{J}_{\mathbf{x}\psi t}\dot{\mathbf{\Psi}}_t \tag{7} $$

Where the task space velocity $\dot{\mathbf{x}}_t$ is a twist vector with the linear velocity preceding the angular velocity.

$$
\mathbf{J}_{\mathrm{x}\psi t}=\begin{bmatrix}
l_t\cos\delta_t\left(\dfrac{\cos\theta_t-1}{\theta_t^2}+\dfrac{\sin\theta_t}{\theta_t}\right) & l_t\dfrac{\sin\delta_t}{\theta_t}\left(\cos\theta_t-1\right)\\
l_t\sin\delta_t\left(\dfrac{1-\cos\theta_t}{\theta_t^2}-\dfrac{\sin\theta_t}{\theta_t}\right) & l_t\dfrac{\cos\delta_t}{\theta_t}\left(\cos\theta_t-1\right)\\
l_t\dfrac{\theta_t\cos\theta_t-\sin\theta_t}{\theta_t^2} & 0\\
\sin\delta_t & \cos\delta_t\sin\theta_t\\
\cos\delta_t & -\sin\delta_t\sin\theta_t\\
0 & \cos\theta_t-1
\end{bmatrix} \tag{8}
$$

$$
\lim_{\theta_t\to 0}\mathbf{J}_{\mathrm{x}\psi t}=\begin{bmatrix}
\dfrac{l_t\cos\delta_t}{2} & -\dfrac{l_t\sin\delta_t}{2} & 0 & \sin\delta_t & \cos\delta_t & 0\\
0 & 0 & 0 & 0 & 0 & 0
\end{bmatrix}^T \tag{9}
$$

C. Joint Space Kinematics

According to the geometry of the continuum joint, the j^{th} cable length within the t^{th} joint is formulated as follows:

$$
l_{t\_j}=2\left[\frac{2l_t}{\pi-2\theta_t}-r\cos\left(\delta_t+\left(j-1\right)\beta\right)\right]\sin\left(\frac{\pi-2\theta_t}{4}\right) \tag{10}
$$

Hence, each element of the joint space vector $\mathbf{q}_t$ can be defined as the difference between the target and the initial cable lengths.

V. Experimental Verifications

Experimental characterizations were performed to validate the feasibility of the proposed floating robotic arm design. Motion calibration and actuation compensation strategies were implemented to improve the positioning accuracy of the robotic arm.

A. Design Validation

The bending shape of the nitinol rod was approximately an arc, as shown in Fig. 7. This can help the floating arm realize a higher positioning accuracy.

As illustrated in Fig. 8, buoyancy of each link properly balanced the weight. Under the actuation from the cables, the joints can be bent to move the floating arm to different positions.

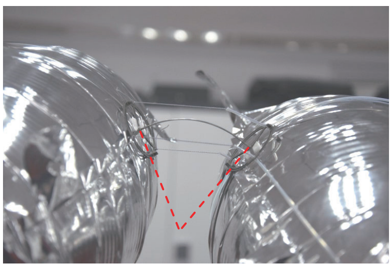

Figure 7. A bent continuum joint with approximately constant curvature

B. Calibration and Actuation Compensation

During the controlled motions of the floating arm, it was found that considerable positioning errors existed. Possible sources of the positioning errors include the following aspects: i) geometrical errors in the arm's construction, and ii) bending discrepancies of the continuum joints. Therefore, motion calibration and actuation compensation is necessary for improved positioning accuracy.

Due to the independent actuation between different joints, the compensation on each continuum joint can be implemented individually. And the calibration thereby focuses on a single 2-DoF continuum joint.

Referring to the existing investigations in [17-19], the compensation was implemented as follows. A joint was first driven according to a desired configuration. Two markers were attached to the adjacent links of the joint and an optical tracker (Micron Tracker, Claron Technology Inc.) was used to quantify the actual bent configuration of the joint. Based on the configuration discrepancy, a fitting curve of the actuation compensation was obtained to correct the bending errors.

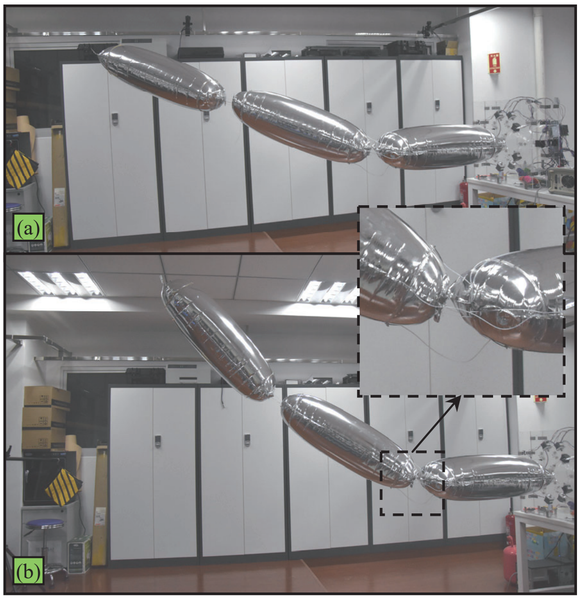

Figure 8. Movement of the 3-link floating robotic arm

For example, the desired θ_t value was set to $\pi/6$, since the maximal bending angle is set at $\pi/3$. The δ_t value was varied from $-\pi$ to π. To achieve the desired θ_t value, the actuation compensation $\Delta\theta_t$ was measured. The compensation mapping from δ_t to $\Delta\theta_t$ was approximately fitted using the following function:

$$
\Delta\theta_t=\sum_{k=1}^{5}\left[a_k\sin\left(b_k\delta_k+c_k\right)\right] \tag{11}
$$

Where a_k, b_k, and c_k are the fitted parameters.

Then the commanded $\tilde{\theta}_t$ was derived as follows

$$
\tilde{\theta}_t=\theta_t+\frac{\theta_t}{\pi/6}\Delta\theta_t \tag{12}
$$

Where $\tilde{\theta}_t$ is the commanded value for the desired bending angle θ_t.

Accuracy was quantified varying the total length of the arm using one to three modules. Since the quantified accuracy involves the arm with different number of modules and hence different lengths, the accuracy is quantified as a ratio of the positioning error to the effective length L_{arm} as in Eq. (13). The positioning error is the average of N = 30 measures with respect to the nominal target point when the robotic arm is actuated with a same configuration $\mathbf{\Psi}_t$.

$$AC = \frac{1}{L_{arm}} \cdot \sqrt{\left(\frac{1}{N}\sum_{i=1}^{N} x_i - x_o\right)^2 + \left(\frac{1}{N}\sum_{i=1}^{N} y_i - y_o\right)^2 + \left(\frac{1}{N}\sum_{i=1}^{N} z_i - z_o\right)^2} \tag{13}$$

Where $[x_i, y_i, z_i]^T$ is the measured position and $[x_o, y_o, z_o]^T$ represents the nominal target position.

The results listed in Table III show the improvements of the robotic arm before and after the actuation compensation when one to three modules were involved.

TABLE III. ACCURACY BEFORE AND AFTER COMPENSATION

Number of modules	Before compensation	After compensation
1	2.89%	1.05%
2	4.88%	2.79%
3	7.90%	4.55%

VI. CONCLUSIONS AND FUTURE WORK

A slim long-reach floating robotic arm is proposed and experimentally verified in this paper, addressing the needs for such manipulators in inspection, detection, search and rescue tasks. The lightweight and compliant design also permits safe human-robot interaction.

Helium Mylar balloons were used to balance the structure's weight, while the acrylic balloon frames and the continuum joints help improve the positioning accuracy. Moreover, decoupled transmission was arranged for simple kinematics.

Preliminary experimental validation shows acceptable positioning accuracy after proper actuation compensation was implemented.

Future work mainly lies on the improvements of the fabrication techniques of the proposed floating arm for more reliable balloon links and more accurate connection between the joint disks and the balloons. Then the control of such a long-reach floating arm in moving air can be investigated.

REFERENCES

[1] V. C. Anderson and R. C. Horn, "Tensor Arm Manipulator." vol. 3,497,083, U. S. P. Office, Ed. United States, 1970.

[2] E. Paljug, T. Ohm, and S. Hayati, "The JPL Serpentine Robot: a 12 DOF System for Inspection," in *IEEE International Conference on Robotics and Automation (ICRA)*, Washington, DC, 1995, pp. 3143-3148.

[3] A. Wolf, H. B. Brown, R. Casciola, A. Costa, M. Schwerin, E. Shamas, and H. Choset, "A Mobile Hyper Redundant Mechanism for Search and Rescue Tasks," in *IEEE/RSJ International Conference on Intelligent Robots and Systems (IROS)*, Las Vegas, Nevada, 2003, pp. 2889-2895.

[4] D. Mishima, T. Aoki, and S. Hirose, "Development of a Pneumatically Controlled Expandable Arm for Rescue Searches in Tight Spaces," *The International Journal of Robotics Research,* vol. 25, No.1, pp. 103-110, Jan 2006.

[5] S. Voisembert, A. Riwan, N. Mechbal, and A. Barraco, "A Novel Inflatable Robot with Constant and Continuous Volume," in *IEEE International Conference on Robotics and Automation (ICRA)*, Shanghai, China, 2011, pp. 5843-5848.

[6] S. Voisembert, N. Mechbal, A. Riwan, and A. Aoussat, "Design of a Novel Long-Range Inflatable Robotic Arm: Manufacturing and Numerical Evaluation of the Joints and Actuation," *Journal of Mechanisms and Robotics,* vol. 5, No.045001, pp. 1-9, Oct. 2013.

[7] J. M. Á. Palacio, A. Riwan, N. Mechbal, E. Monteiro, and S. Voisembert, "A Novel Inflatable Actuator for Inflatable Robotic Arms," in *IEEE International Conference on Advanced Intelligent Mechatronics (AIM)*, Munich, Germany, 2017, pp. 88-93.

[8] R. Qi, A. Khajepour, W. W. Melek, T. L. Lam, and Y. Xu, "Design, Kinematics, and Control of a Multijoint Soft Inflatable Arm for Human-Safe Interaction," *IEEE Transactions on Robotics,* vol. 33, No.3, pp. 594-609, 2017.

[9] H.-J. Kim, Y. Tanaka, A. Kawamura, S. Kawamura, and Y. Nishioka, "Development of an Inflatable Robotic Arm System Controlled by a Joystick," in *IEEE International Symposium on Robot and Human Interactive Communication (RO-MAN)*, Kobe, Japan, 2015, pp. 664-669.

[10] E. W. Hawkes, L. H. Blumenschein, J. D. Greer, and A. M. Okamura, "A Soft Robot That Navigates Its Environment Through Growth," *Science Robotics,* vol. 2, No.8, July 2017.

[11] E. Y. Yarbasi and E. Samur, "Design and Evaluation of a Continuum Robot with Extendable Balloons," *Mechanical Sciences,* vol. 9, No.1, pp. 51-60, 2018.

[12] M. Takeichi, K. Suzumori, G. Endo, and H. Nabae, "Development of Giacometti Arm with Balloon Body," *IEEE Robotics and Automation Letters,* vol. 2, No.2, pp. 951-957, April 2017.

[13] M. Takeichi, K. Suzumori, G. Endo, and H. Nabae, "Development of a 20-m-long Giacometti Arm with Balloon Body Based on Kinematic Model with Air Resistance," in *IEEE/RSJ International Conference on Intelligent Robots and Systems (IROS)*, Vancouver, BC, Canada, 2017, pp. 2710-2716.

[14] S. Kurumaya, H. Nabae, G. Endo, and K. Suzumori, "Exoskeleton Inflatable Robotic Arm with Thin McKibben Muscle," in *IEEE International Conference on Soft Robotics (RoboSoft)*, Livorno, Italy, 2018, pp. 120-125.

[15] R. J. Webster and B. A. Jones, "Design and Kinematic Modeling of Constant Curvature Continuum Robots: A Review " *International Journal of Robotics Research,* vol. 29, No.13, pp. 1661-1683, Nov 2010.

[16] K. Xu and N. Simaan, "Analytic Formulation for the Kinematics, Statics and Shape Restoration of Multibackbone Continuum Robots via Elliptic Integrals," *Journal of Mechanisms and Robotics,* vol. 2, No.011006, pp. 1-13, Feb 2010.

[17] N. Simaan, K. Xu, A. Kapoor, W. Wei, P. Kazanzides, P. Flint, and R. H. Taylor, "Design and Integration of a Telerobotic System for Minimally Invasive Surgery of the Throat " *International Journal of Robotics Research,* vol. 28, No.9, pp. 1134-1153, 2009.

[18] J. Ding, R. E. Goldman, K. Xu, P. K. Allen, D. L. Fowler, and N. Simaan, "Design and Coordination Kinematics of an Insertable Robotic Effectors Platform for Single-Port Access Surgery," *IEEE/ASME Transactions on Mechatronics,* vol. 18, No.5, pp. 1612-1624, Oct 2013.

[19] K. Xu, J. Zhao, and M. Fu, "Development of the SJTU Unfoldable Robotic System (SURS) for Single Port Laparoscopy," *IEEE/ASME Transactions on Mechatronics,* vol. 20, No.5, pp. 2133-2145, Oct 2015.